

Effect of the axial scraping velocity on enhanced heat exchangers



D. Crespi-Llorens^{a,*}, P. Martínez^b, P. Vicente^b, A. Viedma^a

^aDep. Ing. Térmica y de Fluidos, Universidad Politécnica de Cartagena, Dr. Fleming s/n, 30202 Cartagena, Spain

^bDep. Ing. Mecánica y Energía, Universidad Miguel Hernández, Av. Universidad s/n, 03202 Elche, Spain

ARTICLE INFO

Article history:

Received 4 December 2012

Received in revised form 10 June 2013

Accepted 15 June 2013

Available online 19 July 2013

Keywords:

Heat transfer enhancement

Visualization study

Turbulence level

Numerical simulation

SSHE

ABSTRACT

The flow pattern within an enhanced tubular heat exchanger equipped with a reciprocating scraping device is experimentally analysed. The insert device, specially designed to avoid fouling and to enhance heat transfer, has also been used to produce ice slurry. It consists of several circular perforated scraping discs mounted on a coaxial shaft. The whole is moved alternatively along the axial direction by a hydraulic cylinder.

The phase-averaged velocity fields of the turbulent flow have been obtained with PIV technique for both scraping semi-cycles. Special attention has been paid to the effect of the non-dimensional scraping velocity and the Reynolds number in the flow field. CFD simulations provide support for the identification of the flow patterns and the parameter assessment extension.

The results show how the scraping parameters affect the turbulence level produced in the flow and therefore the desired heat transfer enhancement.

© 2013 Elsevier Inc. All rights reserved.

1. Introduction

Insert devices have been deeply investigated (Webb, 2005) in order to improve their efficiency: heat transfer vs. pressure drop. Heat transfer enhancement techniques can be classified into *active* and *passive*. The *passive* ones, like inserted wire coils or mechanically deformed pipes, have been studied for the last 30 years and have become commercial solutions. Webb deduced from his work that *active* techniques can produce very high increases in heat transfer, especially in laminar flow.

The fouling problem of heat exchangers has a significant impact on chemical, petrochemical and food industries. Preventing fouling on heat exchanging devices is essential to avoid heat transfer inefficiencies, corrosion due to deposits formation and pressure loss, which affects the devices' performance (Bergles, 2002).

Mechanically assisted heat exchangers, where a heat transfer surface is periodically scraped by a moving element, might be used to increase heat transfer and avoid fouling. Equipment with rotating scraping blades is found in commercial practice: these devices prevent fouling and promote mixing and heat transfer. Many investigations have focused on these anti-fouling devices, studying flow pattern characteristics (Wang et al., 1999), their thermo-hydraulic performance (De Goede and De Jong, 1993) or scraping efficiency (Sun et al., 2004).

A particular case of fouling problem is the generation of ice slurry in heat exchangers with moving scraping devices. By cooling the outer surface of the exchanger, ice crystals are generated in its inner surface, and the moving device scraps the surface periodically to detach the ice from it. The presence of an additive in the aqueous solution reduces the freezing temperature, in order to control the proportion of ice in the solution. Ice slurries are safe, environment friendly and efficient heat transporters with a capacity of up to 150 kJ/kg. Bellas and Tassou (2005) collected their possible applications. Kauffeld et al. (2005) compared diverse ice slurry production techniques. Several researchers have studied the pressure drop and heat transfer characteristics of ice slurry flowing through compact plate heat exchangers (Bellas et al., 2002; Stamatou et al., 2005; Norgaard et al., 2005) as well as through pipe heat exchangers (Bedecarrats et al., 2003; Lee and Lee, 2005; Lee and Sharma, 2006; Illán and Viedma, 2009b,a).

This research focuses on the analysis of the flow structures produced by the scrapers, which will significantly affect the heat transfer process. The work presents a visualization study carried-out on a heat exchanger prototype with a dynamic inserted device. The flow pattern is obtained by employing the Particle Image Velocimetry (PIV) technique and the results are shown and then compared with the flow pattern numerically obtained through a commercial CFD code. The numerical simulation will serve to find the turbulence model that best fits the experimental solution and helps to explain that particular flow pattern.

The active insert device, specially designed to enhance heat transfer and to avoid fouling, can also be used for ice slurry generation. It consists of several discs with six circumferentially

* Corresponding author. Tel.: +34 605230393.

E-mail addresses: damian.crespi@upct.es, damiancrespi@yahoo.es (D. Crespi-Llorens).

Nomenclature

D	inner diameter of the acrylic pipe (m)
d	diameter of the insert device shaft (m)
D_h	hydraulic diameter $D_h = D - d = 0.028$ (m)
k	turbulent kinetic energy (m^2/s^2)
L	longitudinal position referenced to the centre of the scraper, being positive downstream of it (mm)
N	number of pair of images in an experiment
n	number of pixels in the distance D_h in an image
Q	flow rate (m^3/s)
R	relation between distances in a PIV image, $R = 6928.6$ (pix/m)
r	radial position (m)
s	standard deviation or Root Mean Square function (RMS)
T	temperature ($^\circ\text{C}$)
v	fluid velocity (m/s)
v_b	bulk velocity (m/s)
V	mean velocity component (m/s)
v'	turbulent component of velocity (m/s)
\tilde{v}	random error component of velocity (m/s)

Dimensionless numbers

β	blockage parameter, $\beta = 1 - v_s/v_b$
---------	---

r^*	non-dimensional radial position, $r^* = 2r/(D - d)$
Re	Reynolds number, $Re = \rho v_b D_h / \mu$
v^*	non-dimensional velocity, $v^* = v/v_b$

Greek Symbols

Δt	time elapsed between two consecutive images (s)
Δx	average displacement of the tracing particles contained in an Interrogation Area between the two images of a pair (pix)
μ	dynamic viscosity of the fluid (Pa s)
μ_{eff}	effective viscosity (Pa s)
ρ	density of the fluid, (kg/m^3)
ε	dissipation rate of turbulent kinetic energy (m^2/s^3)

subscripts

co, ct	co-current and counter-current directions
max	maximum value
min	minimum value
s	scraper
y	axial direction

distributed holes on them, which are mounted on a 18 mm diameter coaxial shaft with a pitch of 5D (Fig. 1). The whole is moved alternatively along the axial direction by a hydraulic cylinder. The effects of the Reynolds number and the scraping velocity in the flow will be investigated. Furthermore, the increase of the turbulence level of the flow will be analysed and related to the potential heat transfer increase.

2. Experimental setup

The facility depicted in Fig. 2 was built in order to study the flow pattern induced by a device inserted in the exchanger tube. The main section consists of a 74 mm diameter acrylic tube installed between two reservoir tanks that stabilize the flow.

The test section is located within a distance of 15 diameters from the tube inlet in order to ensure periodic flow conditions. To improve the optical access in this section, a flat-sided acrylic box has been placed. Water is the test fluid chosen for the experiments and is also used to fill the acrylic box. The fluid is pumped through the conducts by a gear pump, regulated by a frequency converter which allows the control of its bulk velocity, measured by an electromagnetic flowmeter. The pump is composed of small gear teeth and in the experiments has always worked at frequencies over 25 Hz to ensure a stable flow. In order to control the fluid temperature, there is an electric heater in the upper reservoir tank. With the rest of the variables fixed, these two parameters determine the Reynolds number. By using water as test fluid at temperatures from 25 $^\circ\text{C}$ to 55 $^\circ\text{C}$ and flow rates of 100–1500 l/h, a Reynolds number range between 400 and 6200 can be obtained.

Particle Image Velocimetry is a broadly used technique which allows us to measure velocity patterns in a flow (Raffel et al., 2000). To that end, the flow is seeded with particles with nearly the same density of the test fluid, in this case 50 μm diameter polyamide particles have been chosen (1.016 kg/l). As shown in Fig. 3a, a laser illuminates flat slices of the flow which contain the axis of the pipe (longitudinal section). The camera is situated in orthogonal position in relation to that plane, so that it can have a front view of it. Taking two consecutive images of the particles and knowing the time gap between them, the 2-dimensional velocity field can be obtained.

The 1 mm thick plane laser light is pulsed at 100–600 Hz in order to obtain multiple pairs of images. Its wavelength is 808 nm. The 1280×1024 pix² CMOS camera, together with a 16X optical zoom lens, provides images with a resolution of 0.14 mm/pix. The camera is controlled by a computer and the camera provides the synchronizing signal to the laser pulse. In the dynamic experiments, the pictures are taken in pairs, triggered by the movement of the scraping device. For each experiment, between 500 and 1000 pairs of images have been processed using the software VidPIV. Cross Correlation (C.C.) and Adaptive Cross Correlation (A.C.C.) algorithms have been used to process the acquired pictures. They have been applied to every pair of images consecutively (Scarano and Reithmuller, 2000), starting with the C.C. with an interrogation area of 32×32 pix² and an overlap of 50%, followed by the A.C.C. algorithm with the same window size and finally repeating the last algorithm with a smaller window size (16×16 pix²). Between the application of each algorithm and in the post-processing, a global velocity filter and an interpolation have been applied, the first one being in charge of eliminating outliers, vectors which are non-consistent with the rest in the field. Finally, results are obtained as an average of the individual results for each pair of images.

The laser light is 1 mm wide and 100 mm high. The PIV technique can only give good results in a region 80 mm high where the illumination quality is optimal. Velocity results are processed in three regions as shown in Fig. 1: Region A, upstream of the scraper, Region B, immediately downstream of the scraper and Region C after Region B, being an overlap of 20 mm between regions B and C. The position of each region is referenced to the scraper position as shown in Fig. 1. 500 pairs of images have been taken in the experiments in region A and 1000 pairs in the experiments in regions B and C.

All the experiments have been repeated at least 3 times to ensure high quality of the final results, which showed high repeatability once the experimental method was properly adjusted.

In dynamic experiments, the insert device has an alternative movement with constant and practically equal velocities in each direction ($|v_{s,co} - v_{s,ct}| < 2\%$), with an amplitude of 200 mm (2.7 D). The shaft is moved by the hydraulic system depicted in Fig. 2. There is a distortion in the movement when changing

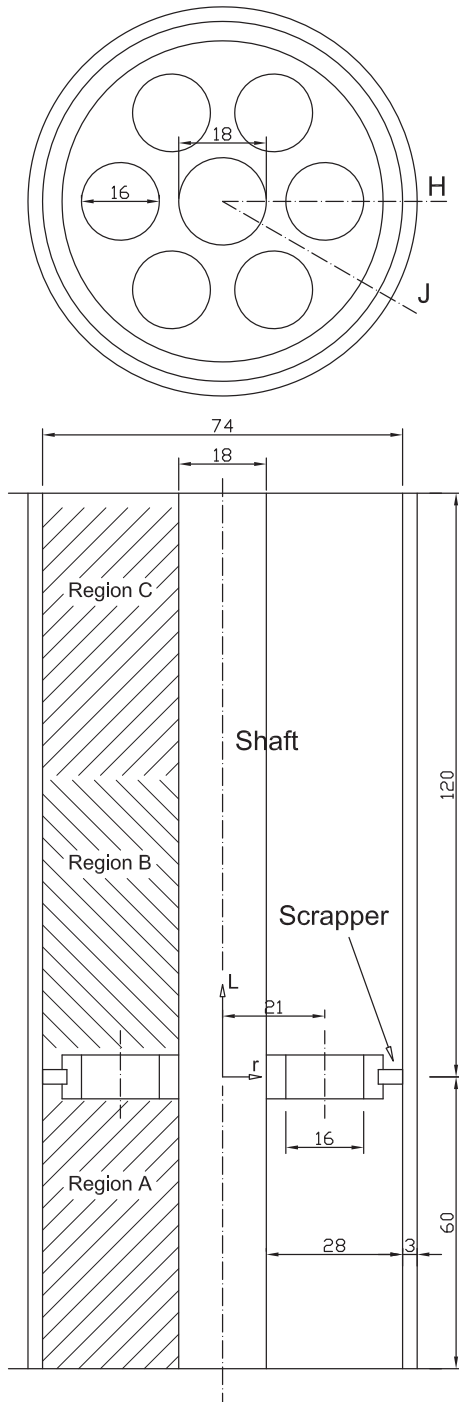


Fig. 1. Sketch of the active insert device analysed.

direction, which does not affect significantly the average velocity of each cycle, being both velocities almost identical but with different sign (see Fig. 3):

$$v_{s,co} = -v_{s,ct} \quad (1)$$

The velocity of the scraper has been measured off-line by an image tracking system, and on-line by two timers (one for each direction).

The two directions of the movement of the insert device will be called, from now on, co-current and counter-current, which relates them to the direction of the flow. The high speed camera is configured to take pairs of pictures in co-current or counter-current direction of the scraper.

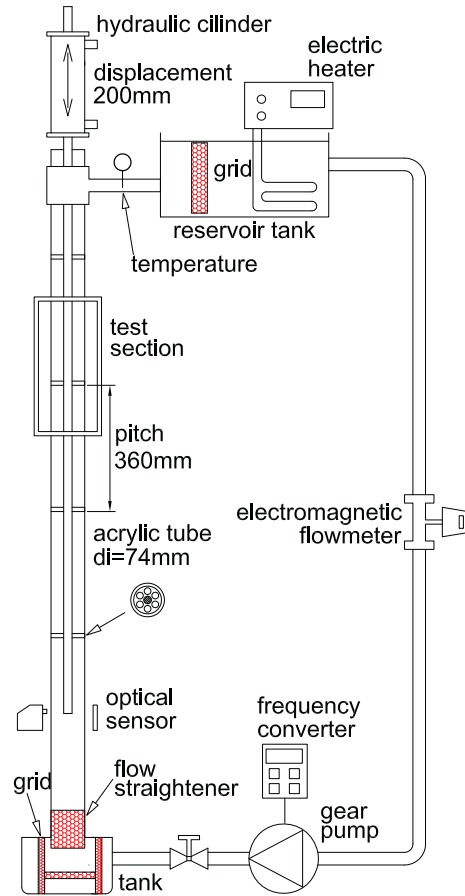


Fig. 2. Sketch of the experimental facility.

The system is triggered by an optical sensor as described in Fig. 3b. The optical sensor is placed in the lower end of the insert device, so that its output signal will change its TTL state from 0 V to 5 V when the insert device shaft is detected and will change back when it goes away. The sensor signal can also be configured with the opposite behaviour. By means of a timer, the signal can be delayed so that the camera shot is triggered exactly when regions A, B or C of the scraper are in position for the image acquisition and the scraper moves in the right direction. When the camera receives the shooting signal, it will take two consecutive images, upload them to the computer and wait until the next shooting signal. This procedure will be repeated 500 times for region A or 1000 times for regions B and C, which can be configured in the commercial software provided by the camera manufacturer. The images of the three regions are taken so that the scraper always appears in them, acting as reference point.

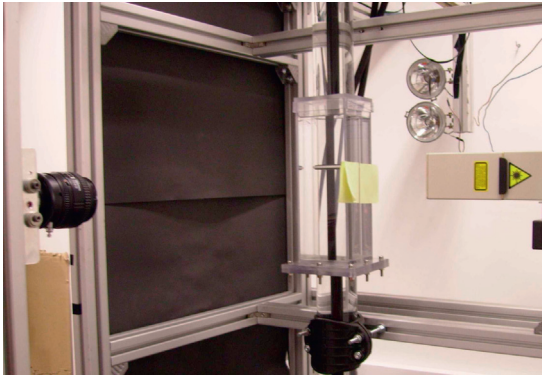
2.1. Accuracy of the experimental data

When obtaining the velocity field out of a pair of images, the velocity at any position is calculated by the PIV algorithm as follows:

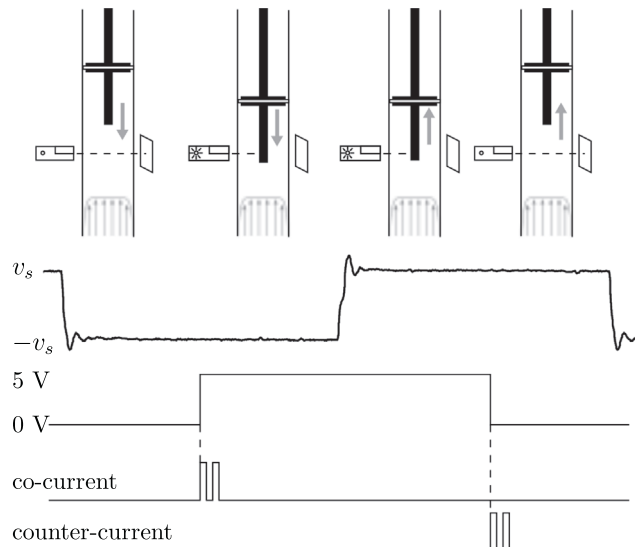
$$v_i = \frac{\Delta x_i}{R \Delta t} \quad (2)$$

$$R = n/D_h \quad (3)$$

The uncertainty associated to the instant velocity can be obtained from Eqs. (4) and (5), where $\partial(\Delta t)$ has been neglected due to the high timing precision of the camera:



(a) Photograph of the PIV facility.



(b) Optical sensor operation. From up to down: optical sensor arrangement, velocity of the scraper, sensor output signal (TTL) and camera shooting signal in the two operation modes (co-current and counter-current).

Fig. 3. PIV system components.

$$\partial(R) = \left[\left(\frac{1}{D_h} \partial(n) \right)^2 + \left(\frac{n}{D_h^2} \partial(D_h) \right)^2 \right]^{1/2} \quad (4)$$

$$\partial(v_i) = \left[\left(\frac{1}{\Delta t R} \partial(\Delta x) \right)^2 + \left(\frac{\Delta x}{\Delta t R^2} \partial(R) \right)^2 \right]^{1/2} \quad (5)$$

When the same physical parameter is measured several times and the result averaged out, the corresponding uncertainty is given by Eq. (6).

$$s(V) = \sqrt{\frac{S^2(v_i)}{N}} \quad (6)$$

If the number of samples is high enough, this uncertainty in the mean estimation is reduced significantly.

The scale factor uncertainty is obtained from Eq. (4), being $\partial(R)/R = 0.0155$. According to Scarano and Reithmuller (2000), if there is no velocity gradient the PIV algorithm estimates the particle displacement with a precision of $\partial(\Delta x) = 0.005$ pix. However, if there is a velocity gradient, an additional error appears, whose maximum value is given by the maximum velocity difference in an interrogation area (16 pix). The latter error has been calculated for the resulting velocity fields of the experiments, its maximum value

Table 1
Experiments in dynamic conditions of the scraper.

Ex.	Q (l/h)	T (°C)	v_b (m/s)	Re	v_s (m/s)	v_s/v_b	β
1	590	30	0.0405	1400	0.02025	0.5	0.5
2	590	30	0.0405	1400	-0.02025	-0.5	1.5
3	590	30	0.0405	1400	0.0405	1	0
4	590	30	0.0405	1400	-0.0405	-1	2
5	371	54	0.0255	1400	0.0510	2	-1
6	371	54	0.0255	1400	-0.0510	-2	3

being $\partial(v_i)/v_b = 0.3$, which corresponds to the area with highest velocity gradient of the experiment number 6 (see Table 1). This error is much bigger than the others and consequently, the uncertainty associated to a single measurement is $\partial(v_i)/v_b \approx \partial(v_i)/v_b = 0.3$.

For the experiments, between 500 and 1000 pair of images have been used. The PIV algorithm is applied to each pair and the results averaged out. Then, the random error is reduced significantly and can be quantified by the standard deviation of the non-dimensional average velocity (Eq. (6)). In the experiments this value is always under $s(V^*) < 0.01$.

2.2. Turbulence contribution to the measured velocity fluctuations

In the case of a turbulent flow, the velocity field is not always the same and it is affected by the turbulent fluctuation. Each measured value of the velocity can be seen as the addition of three components: the mean velocity, the turbulent fluctuation and a random error due to the measuring process.

$$v_i = V_i + v'_i + \tilde{v}_i \quad (7)$$

The estimation of the variance of the turbulent fluctuation can be obtained by subtracting the variance of the measuring error from the variance of the measured data.

$$s^2(v'_i) = s^2(v_i) - s^2(\tilde{v}_i) \quad (8)$$

The value of $s^2(\tilde{v})$ is given by fluctuating errors in the measurements. In this case, the error of the PIV algorithm is due to the velocity gradients, which have been quantified for the whole velocity field in the previous section.

As the turbulent component of the velocity can only be obtained with precision in the axial direction, only one component of the Reynolds stress tensor can be calculated, $\overline{v'_y v'_y}$, which is given by $s^2(v'_i)$ (Eq. (8)).

3. Numerical simulation method

The reciprocating movement of the scrapers creates a remarkable mixing effect between the core region and the flow near the walls resulting in a complex turbulent flow as seen in the PIV technique images. To assist in identifying the underlying flow patterns, a numerical simulation has been conducted for each one of the different experiments, for the static and dynamic conditions of the scraper and under the same conditions of flow rate, Reynolds number, scraping direction and velocity.

To reduce the computation effort, all of the simulations are carried out with a reduced computation domain restricted to the section of the heat exchanger prototype between two consecutive scrapers. Due to the rotational symmetry of the scraper, finally only one-sixth of this domain is taken into account. A periodical boundary is adopted at the inlet and outlet sections in which the fluid parameters are coupled and the side sections of the domain are set as a symmetry condition.

The geometric model accurately reproduces the scraper shape and its rounded edges. A structured mesh is adopted and

hexahedral cells are generated for almost the whole computation domain. Local cell refinement is carefully conducted near the walls for the consideration of the proper y^+ values and to ensure the accuracy of the numerical results in the regions where high velocity gradient is expected.

The numerical simulation of the pipe flow with inserted devices is performed by using the commercial CFD software package Fluent v6.3. A steady incompressible turbulent flow model and double-precision solver are used. The conservation equations of continuity and momentum in the Cartesian coordinate system are presented in the tensor form as follows:

$$\frac{\partial u_j}{\partial x_j} = 0 \tag{9}$$

$$\frac{\partial}{\partial x_j} (\rho u_i u_j) = -\frac{\partial p}{\partial x_i} + \frac{\partial}{\partial x_j} \left[\mu \left(\frac{\partial u_i}{\partial x_j} + \frac{\partial u_j}{\partial x_i} \right) \right] + \frac{\partial}{\partial x_j} (-\rho \overline{u_i u_j'}) \tag{10}$$

The RNG (renormalization group method) $k-\varepsilon$ turbulence model with enhanced wall treatment is adopted for turbulent quantities (Yakhot and Orszag, 1986). This model includes the effect of swirl on turbulence so better accuracy and reliability are expected compared to standard $k-\varepsilon$ model for swirling flows and wall bounded jets (Wang et al., 2011; Aslam Bhutta et al., 2012). The turbulence kinetic energy k and its rate of dissipation ε are obtained from the following transport equations:

$$\frac{\partial}{\partial x_i} (\rho k u_i) = \frac{\partial}{\partial x_j} \left(\alpha_k \mu_{eff} \frac{\partial k}{\partial x_j} \right) + G_k - \rho \varepsilon \tag{11}$$

$$\frac{\partial}{\partial x_i} (\rho \varepsilon u_i) = \frac{\partial}{\partial x_j} \left(\alpha_\varepsilon \mu_{eff} \frac{\partial \varepsilon}{\partial x_j} \right) + C_{1\varepsilon} \frac{\varepsilon}{k} G_k - C_{2\varepsilon} \rho \frac{\varepsilon^2}{k} - R_\varepsilon \tag{12}$$

where G_k represents the generation of turbulence kinetic energy due to mean velocity gradients, α_k and α_ε are the inverse effective

Prandtl numbers for k and ε , μ_{eff} is the effective viscosity and R_ε is an additional term that improves the accuracy for rapidly strained flows. The closure coefficients for the RNG $k-\varepsilon$ model have the following default values (Launder and Spalding, 1972): $C_{1\varepsilon} = 1.42$, $C_{2\varepsilon} = 1.68$, $C_\mu = 0.0845$, $\eta_0 = 4.38$ and $\beta = 0.012$.

Four RANS type turbulence models (standard $k-\varepsilon$, realizable $k-\varepsilon$, RNG $k-\varepsilon$ and Reynolds stress model) have been used and compared in the simulations, according to previous fluid flow studies referenced in the literature for offset and wall jets (Behnia and Nasr, 1996; Li and Zhou, 2007; Li et al., 2009; Chang and Wang, 2012) and swirling pipe flows in heat exchangers with inserted devices (Zhang et al., 2005; Escue and Cui, 2010; Lisboa et al., 2010). The selection and validation of turbulence model is carried out by comparing the predicted velocity field with PIV results. It has been observed that the results obtained by standard $k-\varepsilon$ model are under-predicted in comparison with the experiments for the maximum velocity of the jets at the centre and in general show a more uniform turbulent velocity field. Realizable $k-\varepsilon$ and Reynolds stress models are able to capture the flow features that have been observed in the experiments, but they are found to be less accurate than the RNG $k-\varepsilon$ calculations. So we concluded that the appropriated turbulence model for our type of flow is the RNG $k-\varepsilon$ model and the numerical results obtained are reasonably satisfactory.

In the case of dynamic condition of the scraper and in order to transform the unsteady problem of fluid motion relative to the stationary frame (acrylic tube) into steady with respect to the moving frame (inserted devices with constant translational speed), a moving reference frame (MRF) formulation is adopted in the numerical model, as outlined by Solano et al. (2010) who investigated a similar reciprocating scraped surface heat exchanger.

For the spatial discretization all the variables are treated with the second order upwind scheme, except the pressure, which uses

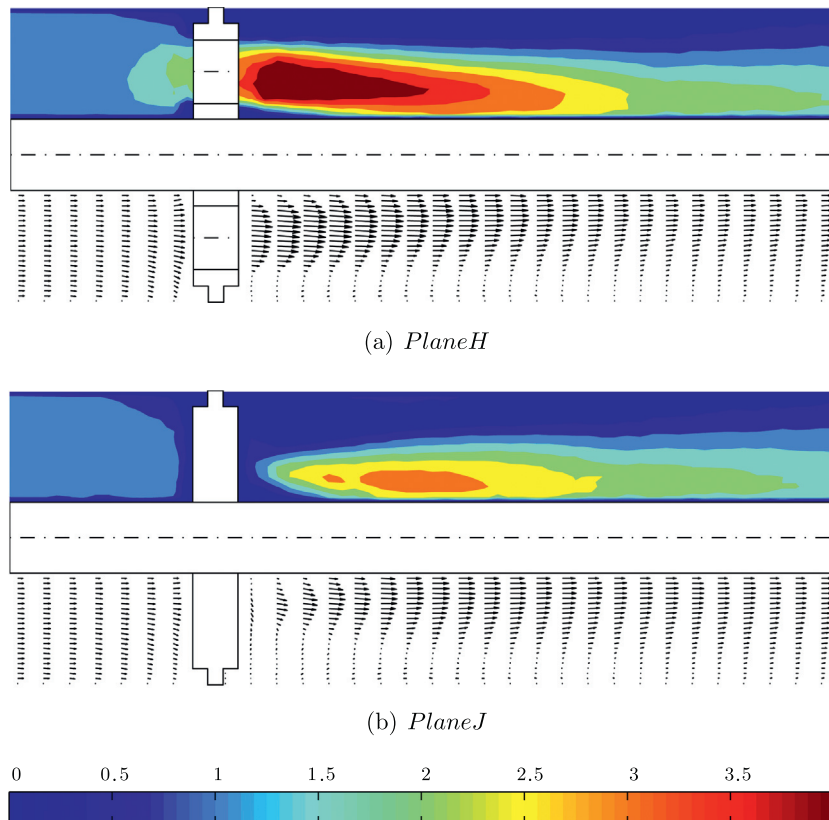


Fig. 4. Assessment of mean flow structures in static conditions. $Re = 4100$. Representation of non-dimensional velocity in axial direction, v_x^* , of PIV measurements. Represented length of the pipe: $-40 \text{ mm} < L < 120 \text{ mm}$.

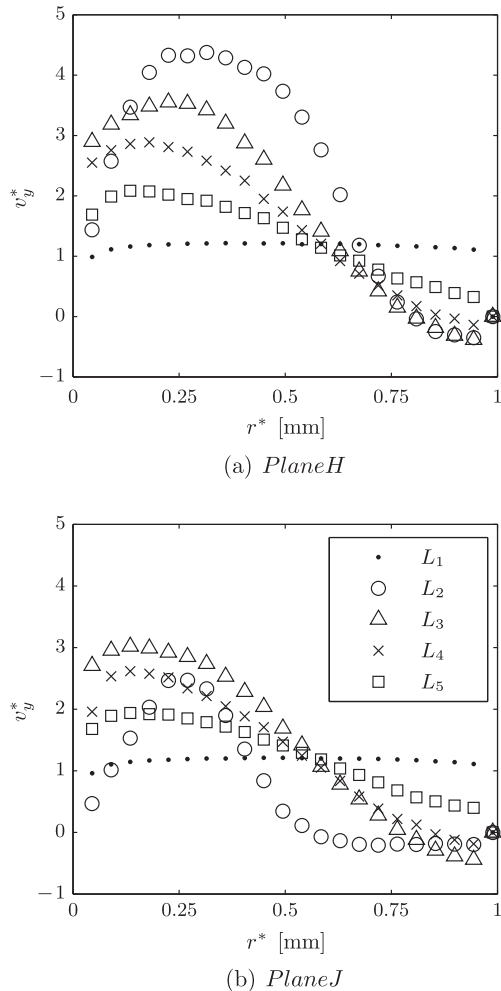


Fig. 5. PIV velocity profiles in static conditions of the scraper, measured at different axial positions: $L_1 = -51$ mm, $L_2 = 20$ mm, $L_3 = 52$ mm, $L_4 = 70$ mm, $L_5 = 115$ mm.

a standard scheme. The pressure-based solver is set for the numerical computations and the SIMPLE algorithm is used for the pressure-velocity coupling. Near-wall regions are modelled with an enhanced wall treatment. The convergence criteria are less than $1e-7$ for the velocity, k and ϵ . The numerical model was validated through some simple simulations of the heat exchanger prototype without inserted devices under the same turbulent flow regime and Reynolds number. Grid independence of the results is checked by varying the number of grid cells, as proposed by Freitas (2002), and taking into account the compromise of computational time and accuracy.

4. Results

4.1. Average flow description in static conditions

The flow pattern has been analysed in static conditions, where the scraper device does not move. The transition from laminar to turbulent regime in this kind of devices under static conditions occurs at $Re \approx 200$ as has been proved by Solano et al. (2010). Experiments have been carried out at different Reynolds numbers, ranging from 1300 to 4100, which ensures a fully turbulent flow. To achieve this, the temperature has been kept constant at 45 °C while varying the flow rate from 400 l/h to 1300 l/h.

Under these conditions, three groups of images have been taken, each one composed of 500–1000 pairs of images. The first

group is made up of pictures of the flow just before the scraper and the other two are located in consecutive positions after it (Fig. 1).

The 2-dimensional images represent a plane of the flow. As this type of flow only has two different symmetry planes, experiments have been carried out on both of them, which are in radial direction. As shown in Fig. 1, the first plane (H) is located crossing each hole of the scraper through its diameter and the second one (J) is situated in the middle of the gap between two consecutive holes.

The behaviour of the fluid in Region B of both symmetry planes (H and J) is resented in Video 1.

Fig. 4 shows the measured velocity fields in both symmetry planes: centre hole (H) and between holes (J). Fig. 4a shows that the flow pattern is similar to a jet flow. The jet produces high velocities downstream of the holes and flow recirculation in the near wall region and in the region between the holes (plane J).

The insert devices produce 6 round jets of 16 mm diameter each. The jets induce a reverse flow of 4–5 jet diameters long (64–80 mm). Figs. 4 and 5 show the evolution of the flow profiles at different axial locations, from 51 mm upstream of the device to 120 mm downstream of the device.

A non-dimensional velocity in axial direction can be defined in terms of the average velocity of the flow:

$$v_y^* = \frac{v_y}{v_b} \quad (13)$$

Then, it can be observed that its maximum value decreases downstream of the scraper (Fig. 5a). At the device exit ($L = 20$ mm) the velocity profile has a pronounced jet shape ($v_{y,max}^* = 4.3$). At a position $L = 52$ mm downstream of the device, the maximum non-dimensional flow velocity is around 3.5 and the velocities in the region close to the shaft are higher. Further downstream the effect of the jet is about to disappear ($v_{y,max}^*(L = 115 \text{ mm}) = 2$).

In the region between holes, a big recirculation is produced by the effect of the jet flow. At about 70 mm downstream of the device, the jet has expanded to the region between holes (plane J) and the flow becomes axisymmetric, having higher velocities next to the shaft. From this point on, the turbulence induces an homogeneous velocity profile. In the near wall region downstream of the scraper the average velocity is, in general, very low in comparison to the bulk velocity, which can produce an undesired accumulation of fouling. Anyway, in practical applications the insert device will be moved sporadically in order to scrap the inner tube surface.

Despite the variation of the Reynolds number in the experiments, results show no significant differences between experiments at $Re = 1300, 2200, 4400$.

In Fig. 6 the numerical results of non-dimensional velocity in axial direction, v_y^* , are compared with the experimental data in order to examine the performance of the numerical model. The numerical simulations are conducted with several turbulence models, including standard $k-\epsilon$ model and RNG $k-\epsilon$ model, to show which turbulence model best represents the flow field. As shown in Fig. 6a the standard $k-\epsilon$ model underestimates the jet flow scale so is no longer used in the remaining simulations. Comparative studies with other RANS turbulent models show that the RNG $k-\epsilon$ model is the one which best reproduces the overall flow field, therefore it has been used in this investigation. Fig. 6b shows how the model accurately represents the jet effect and how the predicted results differ slightly from the measured velocities with a maximum deviation of 3%.

4.2. Average flow description in dynamic conditions

For the description of the flow in dynamic conditions, it will be useful to define the blockage of the flow β , a non-dimensional number defined in terms of the bulk velocity v_b and the velocity of the

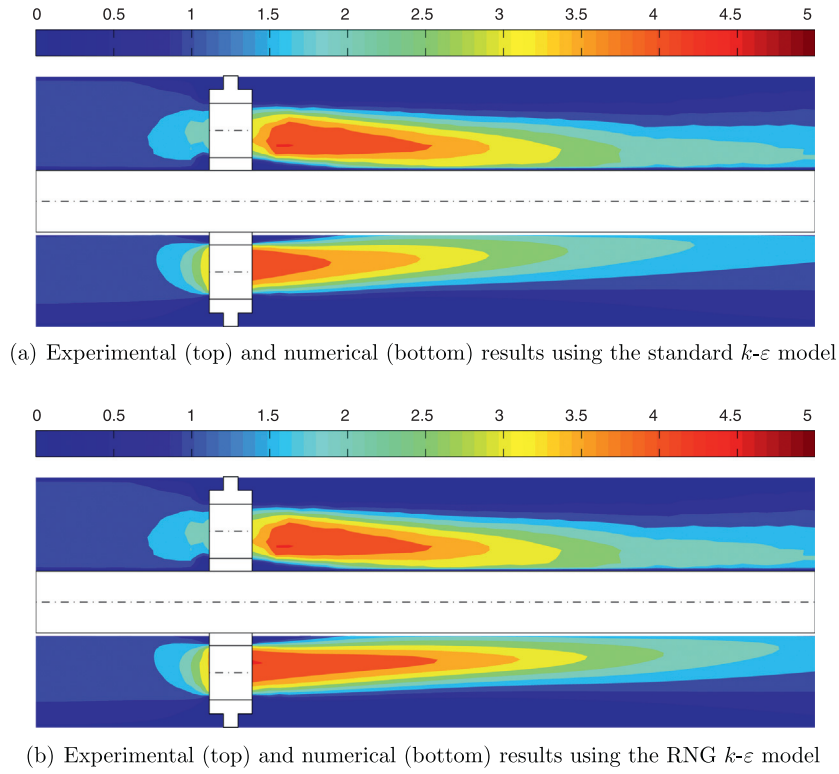


Fig. 6. Comparison of mean flow structures obtained experimentally and numerically in static conditions at $Re = 4100$. Representation of non-dimensional velocity in axial direction, v_x^* . Represented length of the pipe: $-40 \text{ mm} < L < 120 \text{ mm}$.

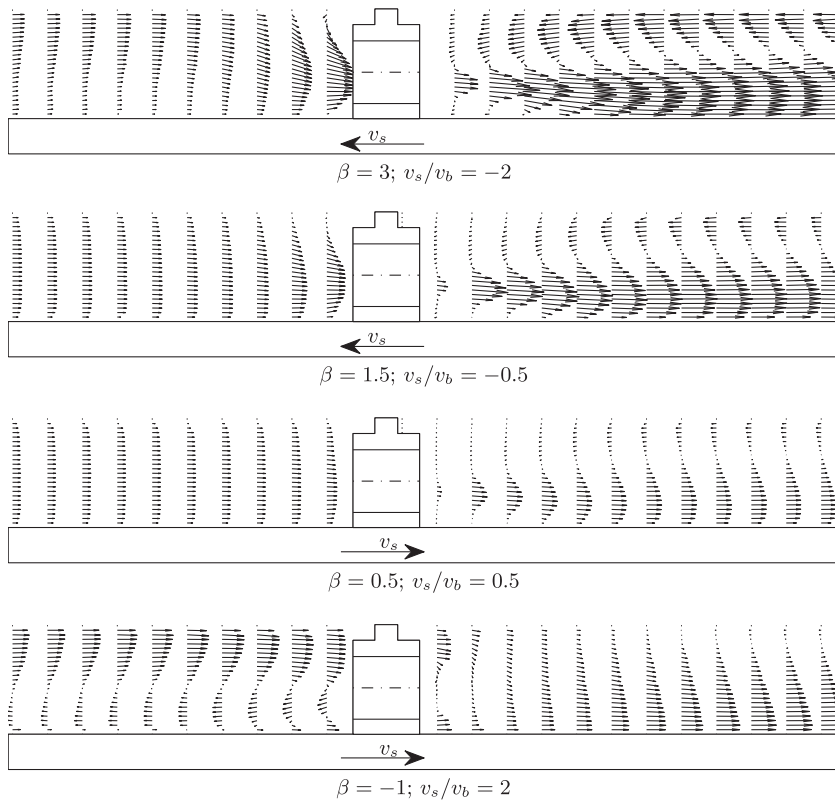


Fig. 7. PIV velocity field along the H symmetry plane at $Re = 1400$. Represented length of the pipe: $-50 \text{ mm} < L < 60 \text{ mm}$.

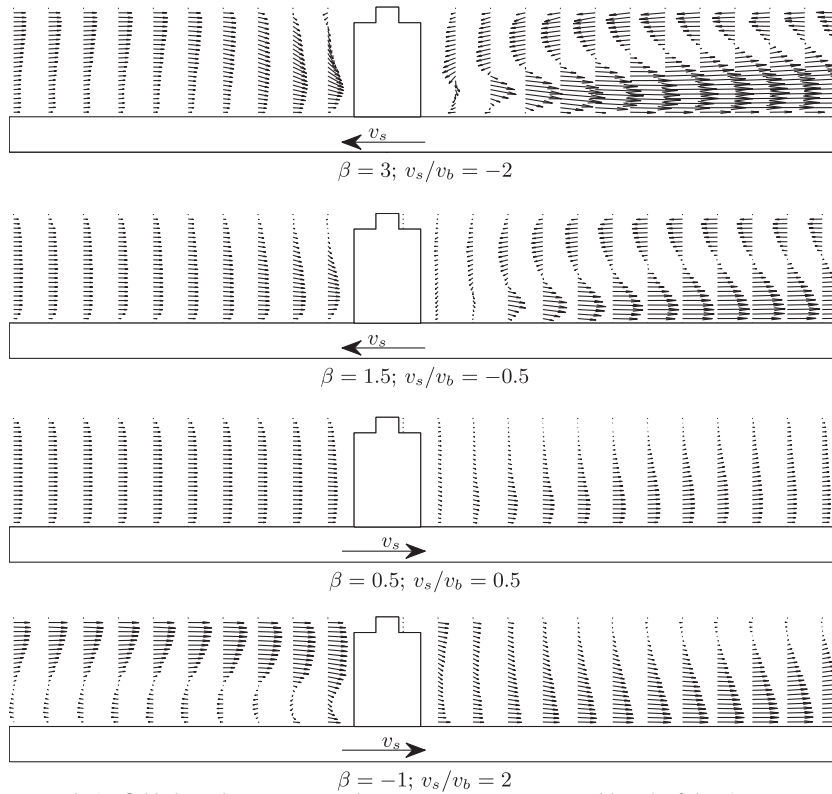


Fig. 8. PIV velocity field along the J symmetry plane at $Re = 1400$. Represented length of the pipe: $-50 \text{ mm} < L < 60 \text{ mm}$.

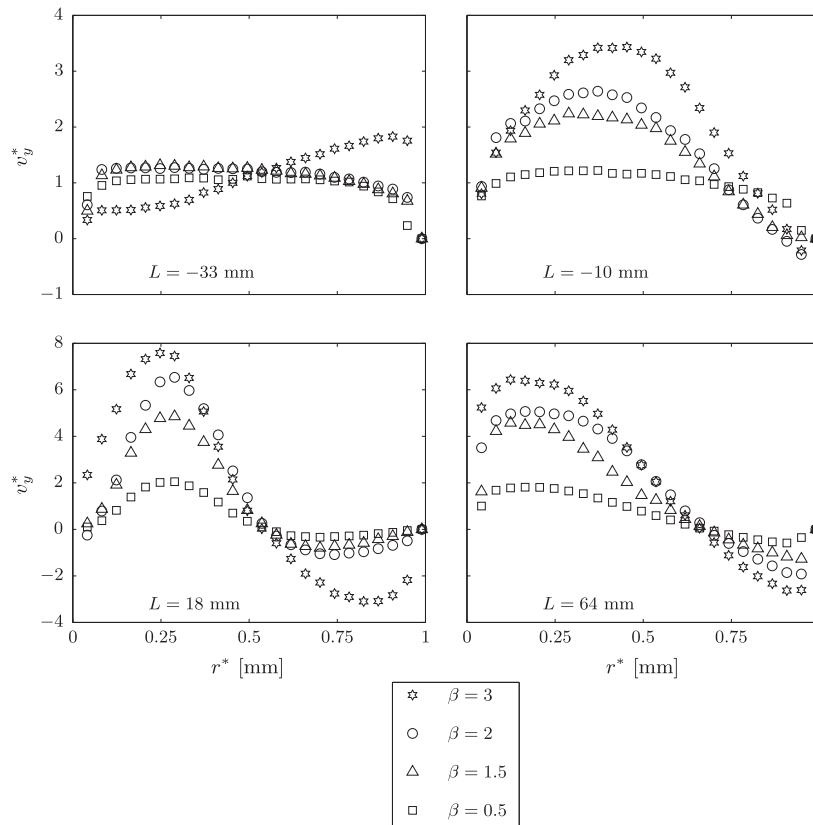


Fig. 9. PIV velocity profiles along the H symmetry plane at $Re = 1400$ and $0.5 < \beta < 3$.

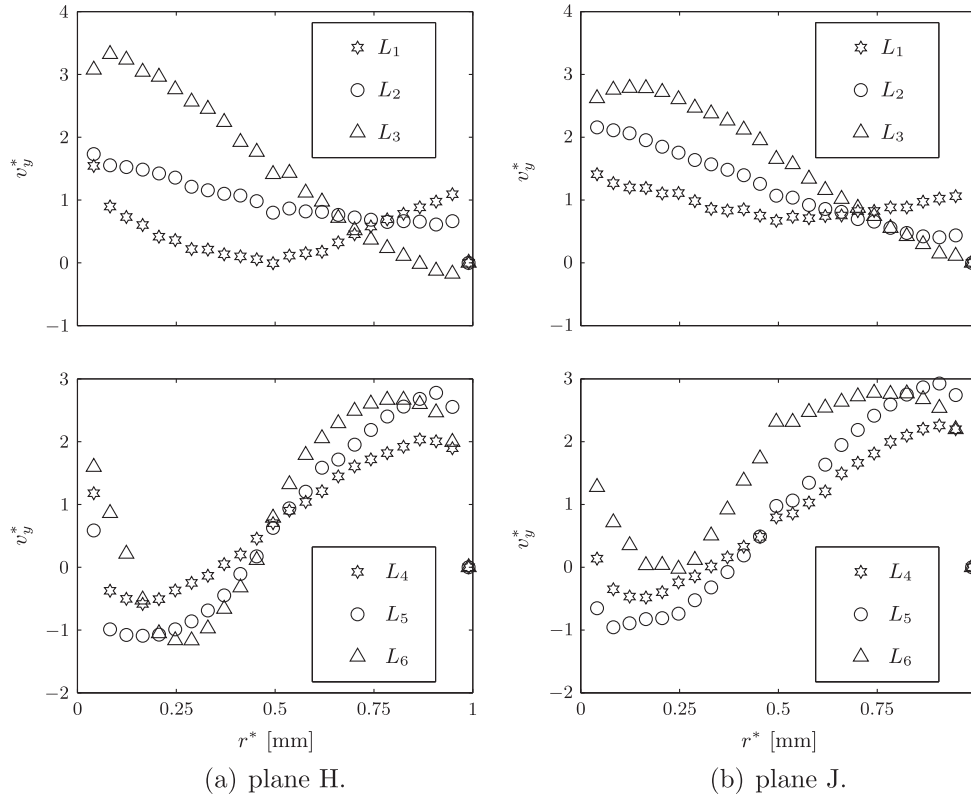


Fig. 10. PIV velocity profiles at $Re = 1400$ and $\beta = -1$. $L_1 = 11$ mm, $L_2 = 21$ mm, $L_3 = 64$ mm, $L_4 = -52$ mm, $L_5 = -31$ mm, $L_6 = -10$ mm.

scraper v_s (Solano et al., 2010). The *blockage* parameter expresses whether the scraper, with its movement, is blocking or helping the fluid flow.

$$\beta = \frac{v_b - v_s}{v_b} = 1 - \frac{v_s}{v_b} \quad (14)$$

- If $v_s < v_b$ then $\beta > 0$ and the scraper is blocking the flow.
- If $v_s > v_b$ then $\beta < 0$ and the scraper is helping the fluid flow.

The bulk velocity always being a positive number ($v_b > 0$), for a counter-flow direction of the scraper movement ($v_s < 0$) and for static conditions ($v_s = 0$) the *blockage* will always be positive ($\beta > 0$). However, when the scraper is moving in co-current direction of the flow ($v_s > 0$), the *blockage* parameter can be positive (for $0 < v_s < v_b$), zero (for $v_s = v_b$) or negative (for $v_s > v_b$).

For this section, experiments have been carried out at five scraping velocities, in co-current and counter-flow directions corresponding to values of $\beta \in [-1, 3]$ (see details in Table 1). The Reynolds number has been kept constant at $Re = 1400$.

An example of the significant effect of the scraper on the flow pattern can be observed in Video 2.

Figs. 7 and 8 depict the non-dimensional velocity field v^* (Eq. (13)) in both symmetry planes of the scraper for $Re_h = 1400$ and β ranging from -1 to 3 . As can be observed, the velocity field depends strongly on the *blockage* phenomenon. As a consequence, the results of the experiments will be grouped according to their *blockage* parameter.

4.2.1. Positive blockage of the flow

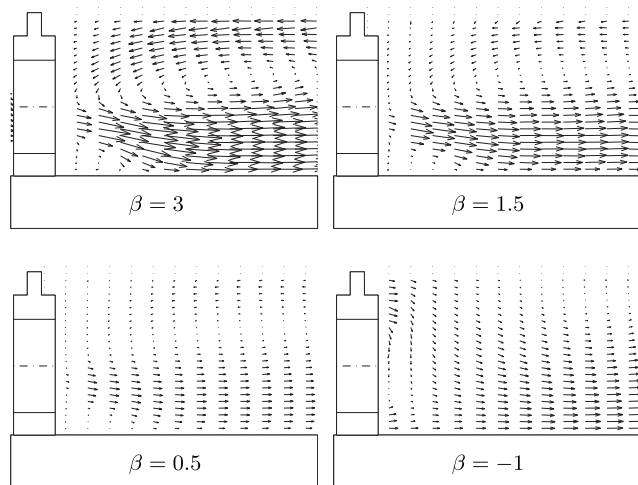
In the experiments where the *blockage* is positive, the velocity pattern is similar in shape to the one obtained in static conditions (Section 4.1). On the one hand, upstream the scraping device, the velocity profile is equal to the one developed in an annulus geom-

etry, and it becomes influenced by the presence of the scraper when coming closer to it. On the other hand, downstream the device, the flow has a *jet* shape, with high positive velocities in the inner region, close to the shaft. In the outer region and the region between the holes, a reverse flow appears, induced by the high velocities in the *jet*.

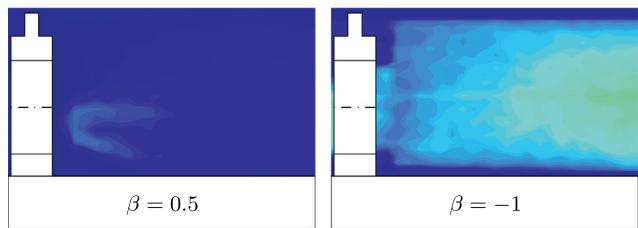
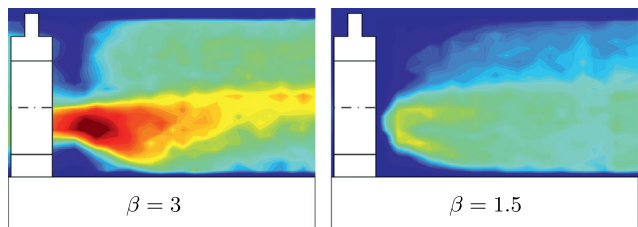
The effect of the scraper in the flow is very similar for all the experiments with $\beta > 0$, but the strength of that effect varies with the value of β . The greater the positive *blockage* parameter, the higher the influence of the scraper. On the contrary, the closer to zero the *blockage* parameter, the lower the influence. These effects can be seen in both symmetry planes, the effects being stronger in plane H which is located in the middle of the *jet*.

For instance, in Fig. 9 it can be observed that upstream the scraper ($L = -10$ mm) the influence of the scraper is hardly appreciable with $\beta = 0.5$ where $v_{y,max}^* = 1.2$ or $\beta = 1$ where $v_{y,max}^* = 1.7$, while in a counter-current motion of the scraper with $\beta = 3$ the effect is significantly stronger $v_{y,max}^* = 3.4$ and it can be observed further from the scraper (see Fig. 7). Downstream of the scraper the strength of the *jet* increases with β , as it can be appreciated in Fig. 9. At the device exit $L = 18$ mm, the maximum non-dimensional velocity in the *jet* has a value of $v_{y,max}^* = 2$ at $\beta = 0.5$, $v_{y,max}^* = 4.3$ at $\beta = 1$, $v_{y,max}^* = 4.9$ at $\beta = 1.5$, $v_{y,max}^* = 6.5$ at $\beta = 2$ and $v_{y,max}^* = 7.5$ at $\beta = 3$. Furthermore, the reverse flow is also higher at $\beta = 3$ than at $\beta = 0.5$, where it can be hardly appreciated. At $L = 18$ mm the maximum velocity in counter-current direction varies from $v_{y,max}^* = -0.3$, at $\beta = 0.5$, to $v_{y,max}^* = -3.1$ at $\beta = 3$. Regarding the total length of the *jet*, it cannot be seen in all the experiments, but it can be safely concluded that it increases with the positive *blockage*.

A secondary difference between experiments with positive *blockage*, is the influence of the movement of the shaft on the velocity profile. This effect is similar to the one which takes place in annulus with a moving shaft. Observing Fig. 7 at positions where the influence of the scraper is low (upstream of the scraper), it can be appreciated that the velocity of the fluid near the moving shaft



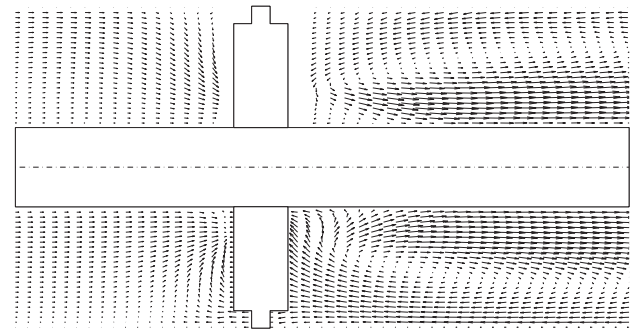
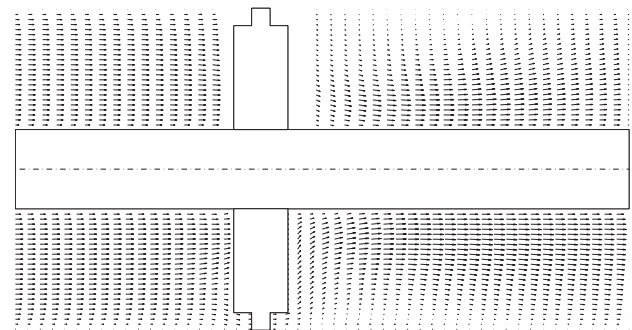
(a) Velocity field.

(b) Non-dimensional RMS value of the turbulent component of the axial velocity, $s(v')/v_b$.**Fig. 11.** PIV details in region A along the H symmetry plane at $Re = 1400$ and four scraping velocities. Represented length of the pipe: $-5 \text{ mm} < L < 60 \text{ mm}$.

is influenced by its movement, being lower when the shaft moves in counter-current direction and higher when it moves in co-current direction, whereas the velocity near the pipe wall suffers the opposite effect.

4.2.2. Negative blockage of the flow

An experiment with negative *blockage* has been carried out in co-current direction and $\beta = -1$. The results depicted in Figs. 7, 8, 10 and 9 show a totally different behaviour from the positive *blockage* experiments. In this case, upstream of the scraper high co-current velocities appear in the outer region of the pipe, reaching a maximum non-dimensional velocity of $v_{y,max}^* = 3$ at $L = -31 \text{ mm}$ (Fig. 10). Besides, in spite of the co-current movement of the shaft, there is a counter-current flow in the inner region ($v_{y,min}^* = -1.3$ at $L = -31 \text{ mm}$). Both effects can be appreciated in planes H and J. On the other side of the scraper, downstream, the velocity profile around $L = 10 \text{ mm}$ in plan H shows higher velocities close to the wall and the shaft, while in between the velocity is nearly perpendicular to the direction of the flow. From $L = 21 \text{ mm}$

(a) Experimental (top) and numerical (bottom) results using the RNG $k-\varepsilon$ model at scraping velocity $\beta = 3$ (b) Experimental (top) and numerical (bottom) results using the RNG $k-\varepsilon$ model at scraping velocity $\beta = 0.5$ **Fig. 12.** Comparison of non-dimensional velocity fields, v_y , along the J symmetry plane obtained experimentally and numerically in dynamic conditions at $Re = 1400$ and two scraping velocities ($\beta = 3, 0.5$). Represented length of the pipe: $-45 \text{ mm} < L < 65 \text{ mm}$.

on, the profile becomes flatter, having higher velocities ($v_{y,max}^* = 2.2$) close to the central moving shaft. Further downstream ($L = 64 \text{ mm}$), the velocities close to the moving shaft have become higher ($v_{y,max}^* = 3.3$) and some reverse flow appears close to the outer wall ($v_{y,min}^* = -0.2$). The effects in plane J downstream of the scraper are very alike, as can be seen in Fig. 10b.

4.3. Turbulence level of the flow

The RMS value of the axial velocity of some of the experiments is depicted in Fig. 11b and the corresponding PIV results in Fig. 11a. The results show a dependence of the turbulence level with the *blockage parameter*. In experiments with a big positive *blockage parameter* ($\beta = 3$), the maximum RMS value of the velocity is high, about $s(v'_i/v_b)_{max} = 4.8$. Its maximum value gets lower when the positive *blockage parameter* decreases, $s(v'_i/v_b)_{max} = 3.2$ for $\beta = 3$, $s(v'_i/v_b)_{max} = 3$ for $\beta = 1.5$ and $s(v'_i/v_b)_{max} = 1.2$ for $\beta = 0.5$. For the experiment with negative *blockage* ($\beta = -1$), $s(v'_i/v_b)_{max} = 1.7$. So it can be concluded that a bigger absolute value of β produces higher turbulence levels in the flow.

4.4. Numerical results

The numerical simulations of the heat exchanger prototype with dynamic inserted devices show an intensive recirculation flow induced by the scrapers that increases the velocity fluctuation in the flow field. The fluid velocity increases downstream through the holes and a remarkable recirculation region is formed behind the scrapers, which leads to considerable enhancement of the mixing effect. Numerical results of non-dimensional velocity fields in Fig. 12 shows that the CFD simulation with the RNG $k-\varepsilon$ model

can be used to accurately predict the flow pattern characteristics of the heat exchanger prototype. The measured and predicted scales for the main recirculations are found to be similar with different *blockage* parameters as shown in Fig. 12a for positive *blockage* and Fig. 12b for negative *blockage*, where a big recirculation region is formed downstream of the scraper and a weaker one emerges upstream of the scraper due to the flow *blockage*. From these comparative studies it can be found that the proposed numerical model can successfully represent the flow performance in heat exchangers with dynamic inserted devices.

5. Conclusions

1. By means of PIV and a computational model, the flow pattern in the tubular enhanced heat exchanger has been obtained for different Reynolds numbers and scraping parameters.
2. Computational and experimental results are in good agreement and the CFD simulation with the RNG $k-\varepsilon$ model is of reasonable precision, so that it can be further used for the cases not supported by experiments.
3. In scraping conditions where the *blockage parameter* is positive, the device produces a *jet* flow which yields to high velocities and large vortex in the region between the holes and in the region close to the wall downstream of the scraper.
4. For a negative value of the *blockage parameter* upstream of the scraper a core of high velocities and a reverse flow in the outer region are produced, while downstream of it high velocities take place in the outer region and a light reverse flow appears in the inner region at some distance from the scraper.
5. High values of the *blockage parameter* yield a significant increase in the turbulence level of the flow, whereas values of β close to zero will cause lower turbulence levels. As a consequence, low values of the *blockage parameter* are to be avoided when selecting the scraping velocity (v_s).

Acknowledgements

The first author thanks the Spanish Government, Ministry of Education for the FPU scholarship referenced as AP2007-03429 which covered the expenses of a 4-year research at *Universidad Politécnica de Cartagena*.

Appendix A. Supplementary material

Supplementary data associated with this article can be found in the online version, at <http://dx.doi.org/10.1016/j.ijheatfluidflow.2013.06.009>.

References

- Aslam Bhutta, M.M., Hayat, N., Bashir, M.H., Khan, A.R., Ahmad, K.N., Khan, S., 2012. CFD applications in various heat exchangers design: a review. *Applied Thermal Engineering* 32, 1–12.
- Bedecarrats, J., Strub, F., Peuvrel, C., Dumas, J., 2003. Heat transfer and pressure drop of ice slurries in a heat exchanger, ICR 0230. In: 21st IIR International Congress of Refrigeration, Washington.
- Behnia, M., Nasr, A., 1996. A comparison of different turbulence models for a plane offset jet. *American Society of Mechanical Engineers, Fluids Engineering Division (Publication) FED* 237, 699–702.
- Bellas, I., Tassou, S.A., 2005. Present and future applications of ice slurries. *International Journal of Refrigeration*.
- Bellas, J., Chaer, I., Tassou, S., 2002. Heat transfer and pressure drop of ice slurries in plate heat exchangers. *Applied Thermal Engineering* 22, 721–732.
- Bergles, A., 2002. ExHFT for fourth generation heat transfer technology. *Experimental Thermal and Fluid Science* 26, 335–344.
- Chang, S., Wang, Y., 2012. Prediction of waterjet performances using $k-\varepsilon$ turbulence models. *Huazhong Keji Daxue Xuebao (Ziran Kexue Ban)/Journal of Huazhong University of Science and Technology (Natural Science Edition)* 40, 88–90+95.
- De Goede, R., De Jong, E., 1993. Heat transfer properties of a scraped-surface heat exchanger in the turbulent flow regime. *Chemical Engineering Science* 48, 1393–1404.
- Escue, A., Cui, J., 2010. Comparison of turbulence models in simulating swirling pipe flows. *Applied Mathematical Modelling* 34, 2840–2849.
- Freitas, C., 2002. The issue of numerical uncertainty. *Applied Mathematical Modelling* 2, 237–248.
- Illán, F., Viedma, A., 2009a. Experimental study on pressure drop and heat transfer in pipelines for brine based ice slurry. *International Journal of Refrigeration* 32, 1808–1814, 1015–1023.
- Illán, F., Viedma, A., 2009b. Prediction of ice slurry performance in a corrugated tube heat exchanger. *International Journal of Refrigeration* 32, 1302–1309.
- Kauffeld, M., Kawaji, M., Egol, P., 2005. *Handbook on Ice Slurries, Fundamentals and Engineering*. International Institute of Refrigeration.
- Lauder, B., Spalding, D., 1972. *Lectures in Mathematical Models of Turbulence*. Academic Press, England.
- Lee, D.W., Lee, S.M., 2005. Pressure drop and heat transfer characteristics of ice slurry in a tube type heat exchanger. In: *Proceedings of the 6th Workshop on Ice Slurries of the International Institute of Refrigeration*, pp. 119–125.
- Lee, D.W., Sharma, A., 2006. Melting of ice slurry in a tube-in-tube heat exchanger. *International Journal of Energy Research* 30, 1013–1021.
- Li, C., Zhou, J., 2007. Experimental and numerical simulation study of heat transfer due to confined impinging circular jet. *Chemical Engineering and Technology* 30, 1355–1361.
- Li, Z., Huai, W., Qian, Z., 2009. Numerical simulation of turbulent radial jets in static ambient. *Shuili Xuebao/Journal of Hydraulic Engineering* 40, 1320–1325.
- Lisboa, P.F., Fernandes, J., Simes, P.C., Mota, J.P.B., Saadatian, E., 2010. Computational-fluid-dynamics study of a kenics static mixer as a heat exchanger for supercritical carbon dioxide. *Journal of Supercritical Fluids* 55, 107–115.
- Norgaard, E., Sorensen, T., Hansen, T., Kauffeld, M., 2005. Performance of components of ice slurry systems: pumps, plate heat exchangers and fittings. *International Journal of Refrigeration* 28, 83–91.
- Raffel, M., Willer, C., Kompenhans, J., 2000. *Particle Image Velocimetry: A practical guide*. Springer.
- Scarano, F., Reithmuller, M., 2000. Advances in iterative multigrid PIV image processing. *Experiments in Fluids* 29, 51–60.
- Solano, J., Garca, A., Vicente, P., Viedma, A., 2010. Flow pattern assessment in tubes of reciprocating scraped surface heat exchangers. *International Journal of Thermal Sciences* 50, 803–815.
- Stamatiou, E., Meewisse, J., Kawaji, M., 2005. Ice slurry generation involving moving parts. *International Journal of Refrigeration*.
- Sun, K., Pyle, D., Fitt, A., Please, C., Baines, M., Hall-Taylor, N., 2004. Numerical study of 2d heat transfer in a scraped surface heat exchanger. *Computers and Fluids* 33, 869–880.
- Wang, B., Miles, P.C., Reitz, R.D., Han, Z., Petersen, B., 2011. Assessment of RNG turbulence modeling and the development of a generalized RNG closure model, in: *SAE 2011 World Congress and Exhibition*.
- Wang, W., Walton, J., McCarthy, K., 1999. Flow profiles of power law fluids in scraped surface heat exchanger geometry using MRI. *Journal of Food Process Engineering* 22, 11–27.
- Webb, R.L., 2005. *Principles of Enhanced Heat Transfer*. Wiley Interscience, The Pennsylvania State University, University Park, PA.
- Yakhot, V., Orszag, S.A., 1986. Renormalization-group analysis of turbulence. *Physical Review Letters* 57, 1722–1724.
- Zhang, L., Qian, H., Xuan, Y., Yu, X., 2005. 3d numerical simulation of fluid flow and heat transfer in self-rotating twisted-tape-inserted tube. *Huagong Xuebao/Journal of Chemical Industry and Engineering (China)* 56, 1633–1638.